Supporting Information

High Thermoelectric Performance in Bi_2Se_2S Compounds via Multi-Element Doping Using Double-Halide Perovskite

Qiu-Yu Luo, Zi-Yuan, Wang, Kun Huang, Chong-Yu Wang, Jing Feng， Yi-Xin Zhang, and Zhen-Hua Ge**

1. Faculty of Materials Science and Engineering, Kunming University of Science and Technology, Kunming, 650093, China.

**Corresponding author: Yi-Xin Zhang* (yxzhang@kust.edu.cn), *Zhen-Hua Ge* (*zge@kust.edu.cn*)

$Cs_3Bi_2I_6Cl_3$ was synthesized according to the reported procedure. X-ray diffraction (XRD) analysis revealed that all diffraction peaks agreed well with the standard PDF card.

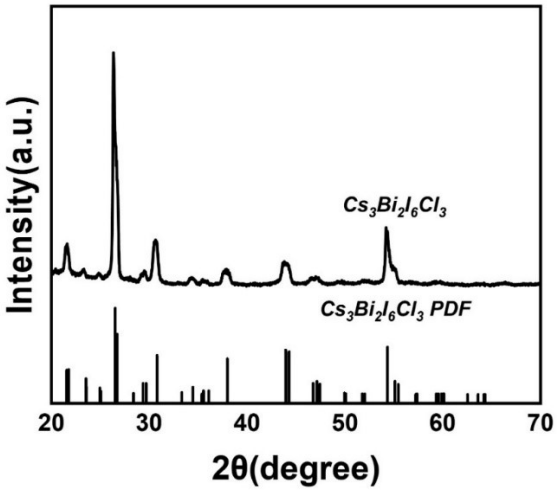

Fig. S1 XRD pattern of synthesized $Cs_3Bi_2I_6Cl_3$.

As shown in Figure S2, both electrical and thermal conductivities in this manuscript were measured parallel to the SPS pressing direction. This orientation was determined based on our previous research, which indicated that the performance along this axis is superior to that perpendicular to the applied pressure.

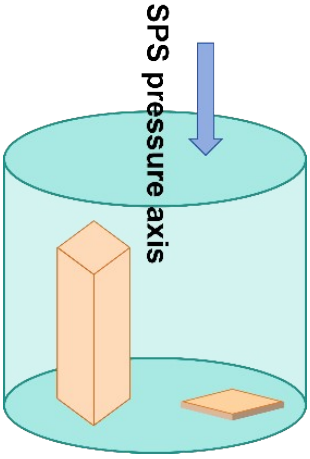

Fig. S2 Schematic illustration of the relationship between electrical/thermal conductivity measurement directions and the SPS pressing axis in the Bi_2Se_2S.

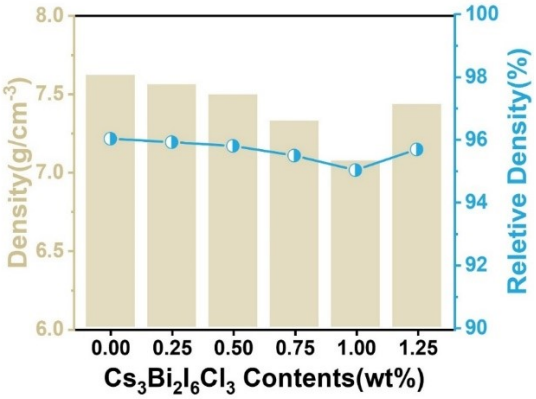

Fig. S3 Density and relative density of different $Cs_3Bi_2I_6Cl_3$ doping concentrations.

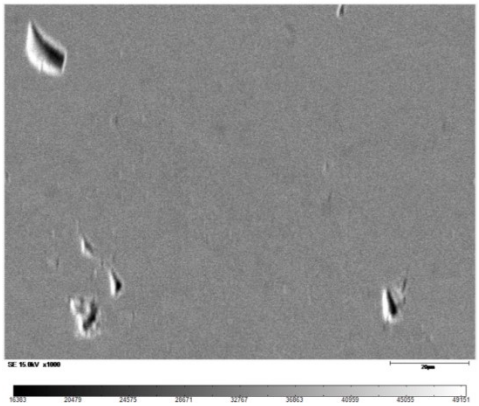

Fig. S4 Backscattered electron (BSE) image of the polished surface of the Bi_2Se_2S-1.00 wt.% $Cs_3Bi_2I_6Cl_3$ sample.

Further scanning analysis was performed on various positions of the Bi_2Se_2S-1.00 wt.%

$Cs_3Bi_2I_6Cl_3$ sample. The resulting Energy-dispersive spectroscopy (EDS) element mapping strongly confirms the homogeneous distribution of all constituent elements within the matrix.

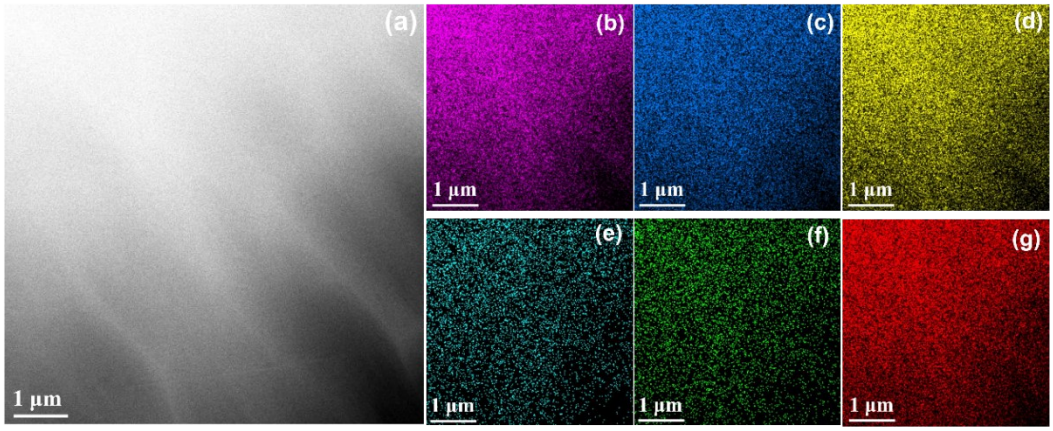

Fig. S5 Energy-dispersive spectroscopy (EDS) of another microscopic region of the Bi_2Se_2S-1.0wt.% $Cs_3Bi_2I_6Cl_3$ sample.

To further elucidate the microstructural origin of the reduced carrier mobility at high doping levels, a quantitative thresholding analysis of the secondary phases was performed using ImageJ software based on the SEM images. As shown in Fig. S6, the 1.00 wt.% sample exhibits a highly homogeneous matrix with negligible secondary phase precipitation. In contrast, when the doping level reaches 1.25 wt.%, distinct secondary phases segregate from the matrix. The quantitative analysis reveals that the area fraction of these segregated phases significantly increases to 1.45%. This visual evidence confirms that the 1.25 wt.% doping exceeds the solid solubility limit, leading to dense phase boundaries that severely scatter charge carriers.

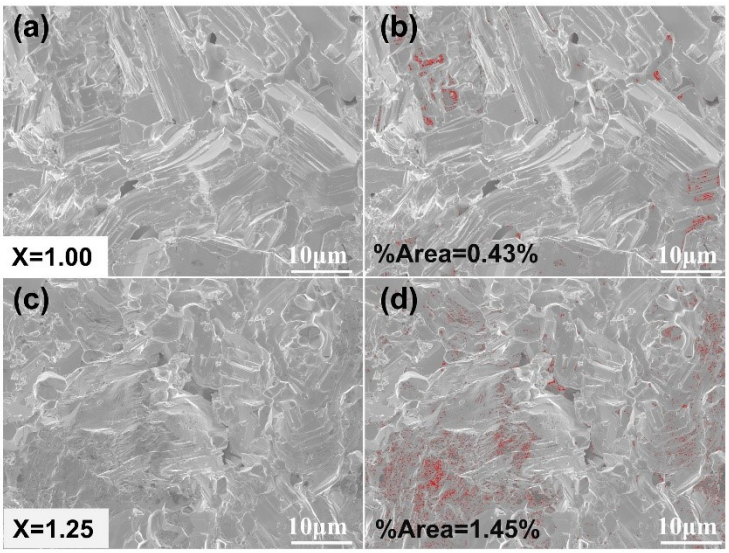

Fig. S6 (a, b) SEM images and (c, d) the corresponding ImageJ thresholding quantitative analysis of the Bi_2Se_2S-1.00 wt.% $Cs_3Bi_2I_6Cl_3$ and Bi_2Se_2S-1.25 wt.% $Cs_3Bi_2I_6Cl_3$ samples. The red-highlighted regions represent the segregated secondary phases.

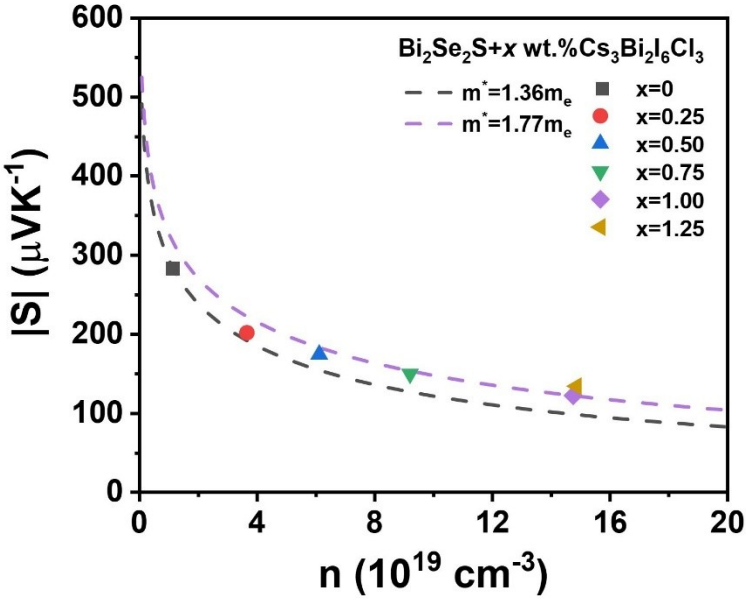

Fig. S7 Absolute values of S as a function of carrier concentration at room temperature.

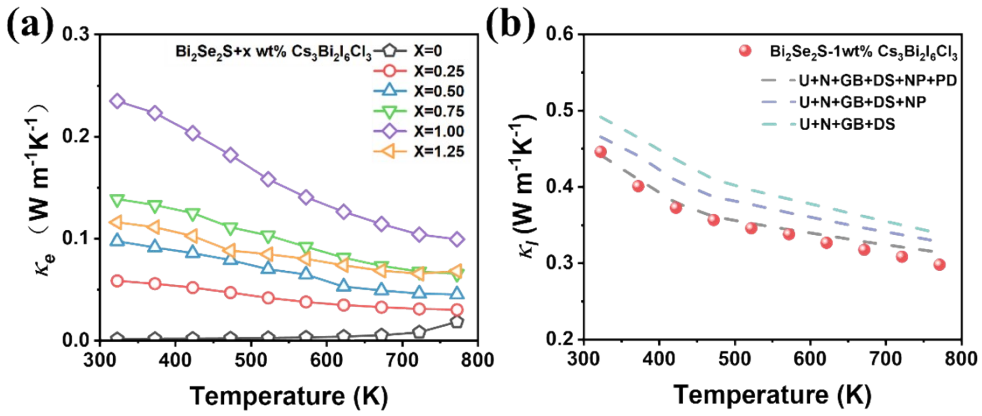

Fig. S8 Bi_2Se_2S+ x wt.% $Cs_3Bi_2I_6Cl_3$(x=0.00, 0.25, 0.50, 0.75, 1.00 and 1.25).(a) Electronic thermal conductivity,(b)Simulated lattice thermal conductivity by considering various scattering mechanisms.

Debye-Callaway's model

To investigate the influence of various scattering mechanisms on the lattice thermal conductivity, the Debye-Callaway model was employed. The specific mathematical expression of this model is presented below:

$$\kappa_s = \frac{k_B}{2\pi^2 v}\left(\frac{k_B T}{\hbar}\right)^3 \int_0^{\frac{\theta_D}{T}} \frac{x^4 e^x}{\tau_c^{-1}\left(e^x - 1\right)^2} dx \#(S1)$$

The parameters in the above expression are defined as follows: x is a dimensionless parameter, which is specifically defined by the ratio $\hbar\omega/k_B T$. Here, k_B denotes the Boltzmann constant, θ_D corresponds to the Debye temperature, $\hbar$ refers to the reduced Planck constant, v represents the average phonon group velocity, ω is the phonon angular frequency. τ_C is the total relaxation time, which follows Matthiessen's rule as:

$$\tau_c^{-1} = \tau_{U-N}^{-1} + \tau_{GB}^{-1} + \tau_{NP}^{-1} + \tau_{DS}^{-1} + \tau_{PD}^{-1} \#(S2)$$

In the model calculation, the influence of the Umklapp and Normal processes on the phonon relaxation time can be described by the following expression for τ_{U-N}^{-1}:

$$\tau_{U-N}^{-1} = A\frac{2\,k_B\tilde{V}^{\frac{1}{3}}\gamma^2\omega^2}{\left(6\pi^2\right)^{\frac{1}{3}}\tilde{M}v^3}T\#(S3)$$

here A is a fitting coefficient, $\tilde{V}$ is the atomic volume of Bi_2Se_2S, γ is the Grüneisen parameter, $\tilde{M}$ is the average atomic mass.

The contribution of boundary scattering to the relaxation time is presented as follows:

$$\tau_{GB}^{-1} = \frac{v_a}{L}\#(S4)$$

where L is the average grain size.

The scattering mechanisms of dislocations can be categorized into strain field scattering and core scattering, which can be respectively described as follows:

$$\tau_{DC}^{-1} = N_D\frac{\tilde{V}^{\frac{4}{3}}}{v^2}\omega^3\#（S5）$$

$$\tau_{DS}^{-1} = 0.6B_D^2N_d(\gamma+\gamma_1)^2\omega\left[\frac{1}{2}+\frac{1}{24}\left(\frac{1-2r}{1-r}\right)^2\{1+\sqrt{2}\left(\frac{v_l}{v_t}\right)^2\}^2\right]\#(S6)$$

Where B_D is the magnitude of effective Burgers vector, *r is* the Poisson ratio, γ and γ_1 are Gruneisen parameter and change in Gruneisen parameter, respectively.

The presence of Cs, Cl and I atoms also induces fluctuations in mass and lattice parameters, which consequently leads to point-defect scattering of phonons. The relaxation time for point-defect scattering is given as follows:

$$\tau_{PD}^{-1} = \frac{V\omega^4}{4\pi v_a^3}\Gamma\#(S7)$$

Where Γ is the scattering parameter related to mass (ΔM) and lattice constant (Δa) differences between two constituents of an alloy. Further research findings confirm that the scattering effect of

point defects is the primary mechanism leading to the significant reduction in the alloy's lattice thermal conductivity.

To evaluate the thermal and structural stability of the optimized Bi_2Se_2S-1.00 wt.% $Cs_3Bi_2I_6Cl_3$ sample, repeated heating-cooling cycle tests were conducted between 323 K and 773 K. The electrical conductivity exhibited a minor decrease, which is attributed to the slight volatilization of halide elements and the accumulation of micro-stress induced defects at elevated temperatures. Nevertheless, both the Seebeck coefficient and lattice thermal conductivity remained stable. Consequently, the *ZT* values was maintained at approximately 0.9, confirming the excellent reliability of the multi-element doping strategy for high-temperature applications. Fig. S9 SEM images of the Bi_2Se_2S-1.00 wt.% $Cs_3Bi_2I_6Cl_3$ sample (a) before and (b) after thermal cycling between 323 K and 773 K.

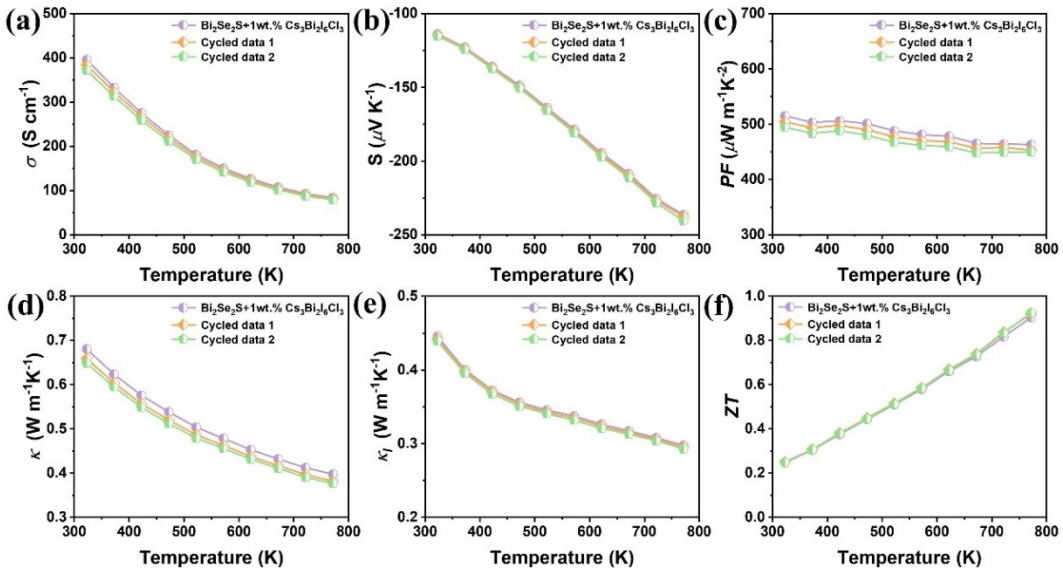

Fig. S9 High-temperature transport stability of the Bi_2Se_2S-1.00 wt.% $Cs_3Bi_2I_6Cl_3$ sample during repeated thermal cycles:(a) electrical conductivity, (b) Seebeck coefficient, (c) power factor,(d) total thermal conductivity,(e) lattice thermal conductivity, (d) *ZT* values.

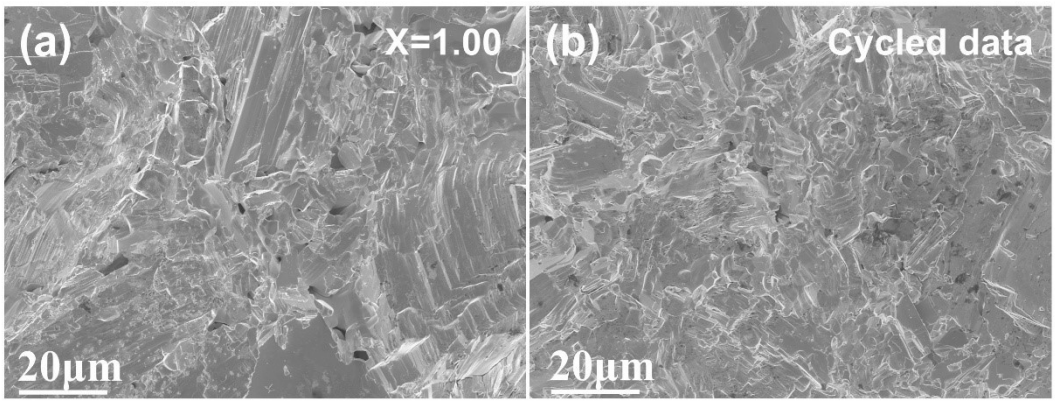

Fig. S10 SEM images of the Bi_2Se_2S-1.00 wt.% $Cs_3Bi_2I_6Cl_3$ sample (a) before and (b) after thermal cycling between 323 K and 773 K.